Geophysical Research Letters

RESEARCH LETTER
10.1029/2020GL090866

Sea Ice Thickness in the Western Ross Sea

Wolfgang Rack[1], Daniel Price[1], Christian Haas[2], Patricia J. Langhorne[3], and Greg H. Leonard[4]

[1]Gateway Antarctica, School of Earth & Environment, University of Canterbury, Christchurch, New Zealand, [2]Alfred Wegener Institute for Polar and Marine Research, Bremerhaven, Germany, [3]Department of Physics, University of Otago, Dunedin, New Zealand, [4]School of Surveying, University of Otago, Dunedin, New Zealand

Key Points:

- Airborne measurements of sea ice thickness in the Western Ross Sea reveal strongly deformed ice with a mean of 2.0 and a maximum of 15.6 m
- Time series of satellite images show evolution and deformation history of polynya-derived pack ice along a total survey length of 800 km
- Sea ice thickness gradients are highest within 100–200 km of polynyas, where the mean thickness of the thickest 10% of ice is 7.6 m

Supporting Information:

- Supporting Information S1

Correspondence to:
W. Rack,
wolfgang.rack@canterbury.ac.nz

Citation:
Rack, W., Price, D., Haas, C., Langhorne, P. J., & Leonard, G. H. (2021). Sea ice thickness in the Western Ross Sea. *Geophysical Research Letters*, *48*, e2020GL090866. https://doi.org/10.1029/2020GL090866

Received 17 SEP 2020
Accepted 25 NOV 2020

Abstract Using airborne measurements, we provide a first direct glimpse of the sea ice thickness distribution in the western Ross Sea, Antarctica, where the distinguishing sea ice process is the regular occurrence of the Ross Sea, McMurdo Sound, and Terra Nova Bay polynyas. Two flights in November 2017 over a length of 800 km reveal a heavily deformed ice regime with a mean thickness of 2.0 ± 1.6 m. Supported by satellite image analysis, we identify regional variability in ice thickness based on formation history. Sea ice thickness gradients are highest within 100 and 200 km of the Terra Nova Bay and McMurdo Sound polynyas, respectively, where the mean thickness of the thickest 10% of ice is 7.6 m. Overall, about 80% of the ice is heavily deformed, concentrated in ridges with thicknesses of 3.0–11.8 m. This is evidence that sea ice is much thicker than in the central Ross Sea.

Plain Language Summary Antarctic sea ice is a stabilizing factor for global climate but has an unknown mass trend as thickness is particularly hard to measure. The western Ross Sea is an important region of sea ice formation; here, persistent off-shore winds form so called coastal polynyas enabling continued freezing by pushing new ice out into the pack ice zone. Using a specialized instrument on a fixed wing aircraft, we measured in this region a mean sea ice thickness of 2 m over a distance of 800 km, which is much thicker than measured in the central Ross Sea. Making use of high-resolution satellite images and aerial photos, we found that narrow deformational ridges grow up to 16 m in thickness and more rapidly than level ice. Such deformed ice holds up to 80% of the ice mass, which is quite easily overlooked by satellite sensors. Our observations hold a link between wind driven ice dynamics and the ice mass exported from the western Ross Sea, which with this new thickness data could be higher than previously thought. Providing this information, we establish a basis for change detection and the evaluation of computer simulations of Antarctic sea ice in a changing climate.

1. Introduction

Sea ice along the Antarctic coastline adjacent to ice shelves and fast ice is a highly sensitive and variable interface between the ocean and the atmosphere (Dale et al., 2017; Tamura et al., 2016). Coastal *latent heat polynyas* are areas of temporarily open water regularly kept free of sea ice by strong off-shore winds (Kern, 2009). High freezing rates make latent heat polynyas focal points of sea ice formation (Ohshima et al., 2016). It is estimated that 10% of the total Southern Ocean sea ice mass is produced in only 1% of the sea ice area by polynya processes (Tamura et al., 2016). Small changes in polynya activity can therefore significantly influence sea ice trends, the formation of High Salinity Shelf Water (HSSW), and Antarctic Bottom Water (Ohshima et al., 2016; Smethie & Jacobs, 2005). Polynya processes play an important role in the development of the ice thickness distribution, as their margins represent areas of dynamic ice deformation (Comiso et al., 2011; Hollands & Dierking, 2016; Nakata et al., 2015).

The western Ross Sea is a notable area for polynya activity as sea ice formation is driven by the complex interaction of three significant polynyas (Dai et al., 2020; Hollands & Dierking, 2016). By supplying a northward drift of sea ice, away from the Ross Ice Shelf, the Ross Sea Polynya (RSP), interrelates closely with the adjacent McMurdo Sound Polynya (MSP) to its west and Terra Nova Bay Polynya (TNBP) to its northwest. The RSP and MSP normally occur simultaneously, as they are caused by strong Ross Air Stream (RAS) events with southerly surface winds split by Ross Island into a western and eastern airflow (Brett et al., 2020; Coggins et al., 2014). The TNBP is a result of katabatic winds, which reach the coast from the East Antarctic plateau channeled through the valleys of the Transantarctic Mountains (Van Woert, 1999). The Ross Sea

sector has experienced the most positive increase in ice extent over the satellite era of 5,800 ± 2,900 km^2 yr^{-1} (Parkinson, 2019) which is thought to have been driven by an increase in meridional winds forced by a change in the synoptics of the wider region (Holland & Kwok, 2012). The ice volume is poorly known, but the proportion of deformed ice as a consequence of wind driven shearing, rafting, and ridging processes can be substantial (Hollands & Dierking, 2016). Springtime assessments using an autonomous underwater vehicle suggest that a large percentage of coastal Antarctic sea ice is strongly deformed and thicker than commonly assumed (Williams et al., 2015).

Estimates of the sea ice thickness in the Ross Sea and the volume flux into the wider Southern Ocean exist (Comiso et al., 2011; Dai et al., 2020), but the sea ice mass balance in the Ross Sea basin is not well quantified (Drucker et al., 2011). The thickness of thin polynya ice can be evaluated from passive microwave and SAR data (Aulicino et al., 2019; Kaleschke et al., 2012), but estimates of thicker ice rely on the freeboard evaluation from satellite altimeters (Kurtz & Markus, 2012; Paul et al., 2018) or aircraft (Tian et al., 2020; Weeks et al, 1989). Satellite observations are only available for intermittent periods and uncertainties of derived ice thicknesses are large because of snow on sea ice and variable sea ice topography (Price et al., 2015, 2019). Nonsatellite-based observations of thickness are still extremely sparse (Worby et al., 2008) but are necessary to validate satellite-based methods (Fons & Kurtz, 2019). Reliable thickness observations are urgently needed to guide model development to assess simulated sea ice volume (Mackie et al., 2020; Uotila et al., 2019).

We describe the first airborne ice thickness measurements over pack ice in the Ross Sea and how the measured ice thickness relates to the observed sea ice morphology as seen in satellite and optical imagery. We evaluate our findings in relation to previous assumptions on ice thickness in the region.

2. Area of Investigation and Datasets

Our study area in the western Ross Sea stretches for 700 km from Ross Island to near Adare Peninsula (72.09°S, 171.53°E; Figure 1). We used an Airborne Electromagnetic Induction (AEM) ice thickness sensor towed by a Basler BT-67 aircraft (Haas et al., 2010) sampling total (ice plus snow) thickness (referred hereafter as ice thickness) every 6 m along the flight track with a signal footprint of 45 m (Haas et al., 2009). The accuracy for ice thickness in the applied measurement set-up is ±0.10 m over level ice (Haas et al., 2009; Pfaffling et al., 2007). However, the maximum thickness of pressure ridges is generally underestimated due to their three-dimensional shape and porosity and the EM footprint diameter of up to 3.7 times the instrument altitude (Reid et al., 2006). The retrieved thickness of unconsolidated ridges can be less than 50% of the "true" thickness (e.g., Haas & Jochmann, 2003). Therefore, obtained thickness distributions are most accurate with respect to their modal thickness and amount of deformed ice, while mean and maximum ice thickness can still be used for relative comparisons between regions (Haas et al., 2010).

Two profiles were flown with a combined length of 800 km (Figure 1c). The Southern Profile was flown from 9 November 2017 22:19 UTC to 10 November 2017 00:25 UTC beginning in McMurdo Sound and went for 300 km to the north, before turning west into Terra Nova Bay for another 100 km. The Northern Profile was flown on 11 November 2017 from 1:21 UTC to 3:04 UTC from the Adare Peninsula in a southerly direction for 215 km before turning southwest toward Cape Washington for another 140 km.

In addition to the ice thickness data, we make use of airborne photography taken from an altitude of 100 m. A Landsat-8 image (panchromatic band at 15 m resolution; 7 November 20:45 UTC) is used to support the interpretation of the sea ice morphology. The ice drift during the week before the survey flights was small (on the order of a kilometer per day), and the Landsat-8 image (Figure S1) was shifted approximately 4 km by coregistration to fit the MODIS image in Figure 1c, which was acquired only a few minutes before the first survey flight.

To provide further context, we make use of auxiliary satellite imagery to reveal the sea ice history over a period of 40 days prior to the AEM survey flights. ESA Sentinel-1 Synthetic Aperture Radar images were acquired (processed to 20 m ground resolution) and used alongside NASA Aqua/Terra corrected reflectance/true color MODIS images (250 m resolution—https://worldview.earthdata.nasa.gov). Small icebergs and sea ice floes of consistent shape are used to manually track sea ice motion to shed light on the formation history of the surveyed ice.

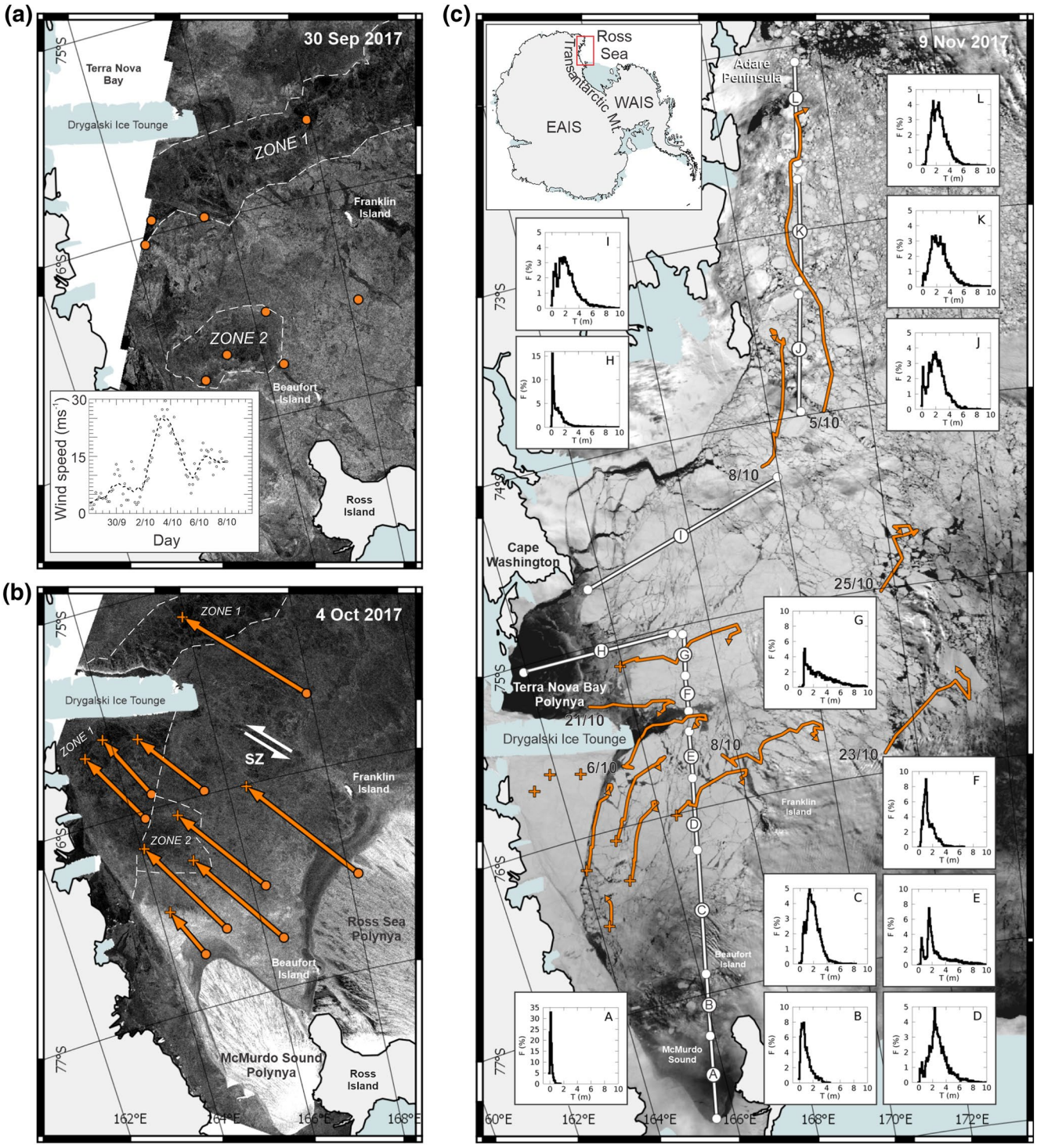

Figure 1. Study region showing ice thickness profiles flown from 9 to 11 November 2017 with ice drift trajectories prior to the airborne survey. (a) and (b) show ice drift between the start (orange dots) and end (orange crosses) of the polynya event plotted on Sentinel-1 SAR images, and (c) shows selected ice drift trajectories (orange with start date if later than 4 October) before the survey flights (white lines) as well as ice thickness histograms of flight sections A to L. Inset in (a) displays 3-hourly mean wind speed from AWS Laurie II.

The 2 October 2017 marks the start of a RAS event that activated the RSP and MSP. Mean 3-hourly surface wind speed upwind of the RSP exceeded 10 m s^{-1} (automatic weather station Laurie II; 77.52°S, 170.81°E) and peaked at about 30 m s^{-1} 2 days later (inset in Figure 1a). Conditions prior to this event are shown in Figure 1a on 30 September which allows us to identify ice floes and begin tracking sea ice drift. There is a gap in useful imagery until the 4 October 2017 marking the final stage of this polynya event (Figure 1b). At this time the RSP and MSP covered an area of about 6,100 km^2 and 3,690 km^2, respectively. The ice drift trajectories shown in Figure 1 are representative for the displacement history in individual sections of the flight tracks. The trajectories south of the Drygalski Ice Tongue (DIT) show two main phases of drift: the extensive mean drift of about 20 km d^{-1} during the 4-day period surrounding the polynya opening (between dots and crosses in Figures 1a and 1b), followed by a much slower and gradual drift over the following 36 days when the polynyas were less active (orange lines Figure 1c). South of Franklin Island, the total ice drift to the northwest between 30 September and 4 October was about 85 km. This pack ice region, with an initial area of 14,000 km^2 was compressed against the DIT, forcing a reduction in area of 50% over this initial 4-day period. This process and the presence of the DIT split a 30 km wide band of pack ice (Zone 1) into two sections, the first into a triangular shaped fast ice area between the southern DIT edge and the continental coast and the second into a pack ice area north of the DIT in Terra Nova Bay (Figure 1b). Two 4 October Sentinel-1 images, acquired 1 h apart, show that ice drift south of DIT had ceased, while the ice to the north was pushed an additional 20 km into Terra Nova Bay creating a Shear Zone (SZ) to the south which is visible as a brighter band of radar reflectivity (Figure 1b). After the 4 October, the compressed pack ice in the northern segment of Zone 1 gradually drifted eastward out of Terra Nova Bay into the Southern flight profile. Further to the southwest around pack ice Zone 2 the polynya event forced slower drift rates of about 64 km over 4 days. West of Beaufort Island the drift turned north and decreased to about 30 km over 4 days about 10 km off the coast. After the polynya event, ice south of the DIT slowly drifted north parallel to the coastline before drifting northeast as it approached the DIT. Upon rounding the terminus of the DIT it was deflected east by the obstructing ice from Terra Nova Bay forming a confluence zone. Just east of the terminus of the DIT, new sea ice formed in between these two zones. This time series of satellite imagery provides context for the deformational history of the pack ice sampled during the flights. A final MODIS image acquired minutes before the southern flight links this image time series to the thickness dataset (Figure 1c). In the following section we discuss the sea ice regime using satellite images to delineate areas with specific sea ice characteristics in support of the statistical analysis.

3. Analysis of Sea Ice Statistics and Volume

The complete Southern and Northern ice thickness profiles and distributions are shown in Figure 2. The length fraction describes the proportion of the profile distance with thicknesses above or below a certain threshold. The cumulative volume fraction is calculated from the histogram by

$$V_k\left(T_k\right) = \frac{\sum_{i=1}^{k} T_i n_i}{\sum_{i=1}^{N} T_i n_i},\ k = 1,2,\ldots,N \tag{1}$$

where $k \le N$ is the number of the kth bin with thickness T_k, n_i the number of observations with thickness T_i, V_k the volume fraction of ice with $T_i \le T_k$, and N the total number of thickness bins.

Drawing on the analysis of distinct ice regions from radar backscattering and drift trajectories as derived from the satellite image sequences, we split the profiles into 12 sections (A to L; Figures 1c and 2). The following measures are presented to characterize the ice thickness statistics (Figure 3 and Table S1); mean thickness with standard deviation (T_{mean}), the most frequently observed ice thickness (T_{mode}), maximum ice thickness (T_{max}), and the mean of the lowest (T_{L10}) and highest (T_{H10}) 10% of measured ice thicknesses. The histograms show non-normal distributions with one or two modes (Figures 1c and 2). Where there is a bimodal ice thickness distribution, two modes (T_{mode1} and T_{mode2}) are determined. The first mode typically represents very young level ice (e.g., refrozen leads), and the second mode represents the older level ice; T_{H10} is a useful statistic to assess pack ice deformation, with larger T_{H10} values suggestive of ice that has been subject to increased ice deformation (Thorndike et al., 1975). Also calculated was the percentage of measurements identified as open water (where ice thickness is <0.10 m), and the volume fraction of deformed ice $V_{D,T} = 1 - V_T$ assuming a threshold thickness T.

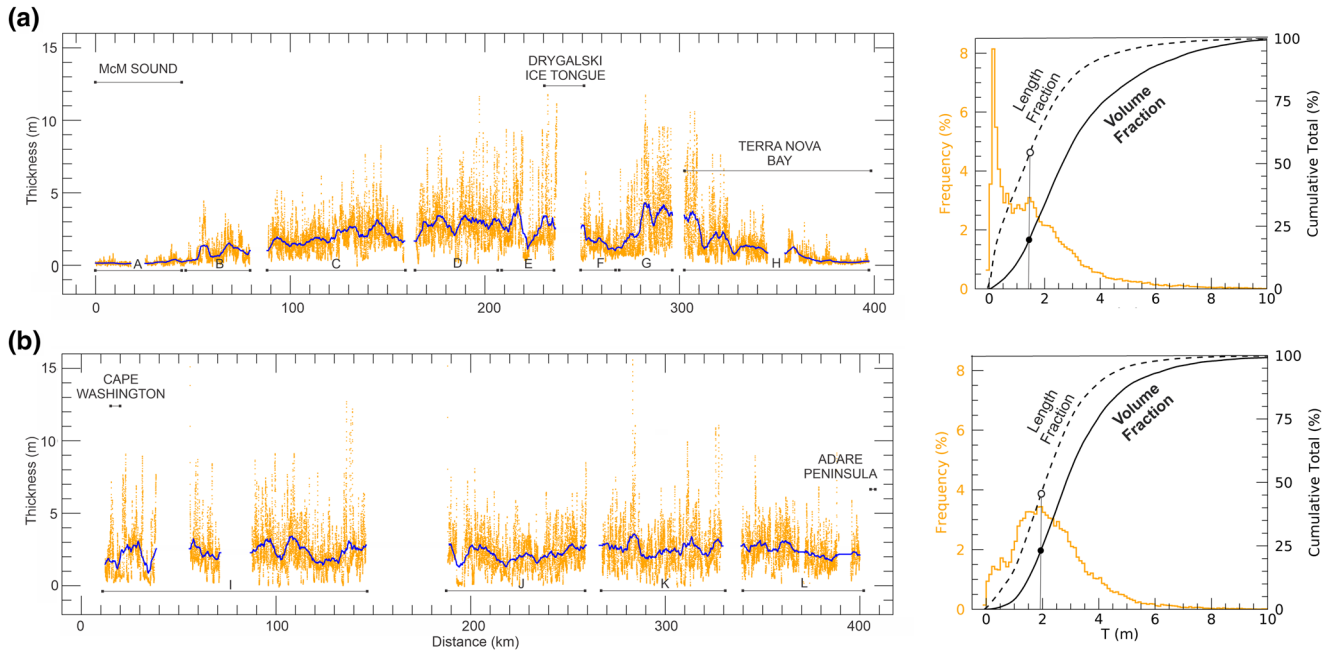

Figure 2. The (a) Southern and (b) Northern ice thickness profiles at full resolution with corresponding histograms (bin size 0.10 m) in the area between McMurdo Sound and Adare Peninsula. The 5 km running mean of ice thickness is shown in blue. For the geographical extent of sections A-L see Figure 1. The vertical line in the histogram marks T_{mode2} for separating fractions of deformed and undeformed ice.

The combined mean sea ice thickness of the two profiles was 1.99 ± 1.57 m with open water representing 2.9% of the measurements. The mean ice thicknesses along the Southern and Northern Profiles were 1.72 ± 1.59 m and 2.35 ± 1.45 m, respectively, with large spatial variations and strong gradients in the mean ice thickness from very thin ice in the polynya areas to much thicker ice in areas that have been subject to

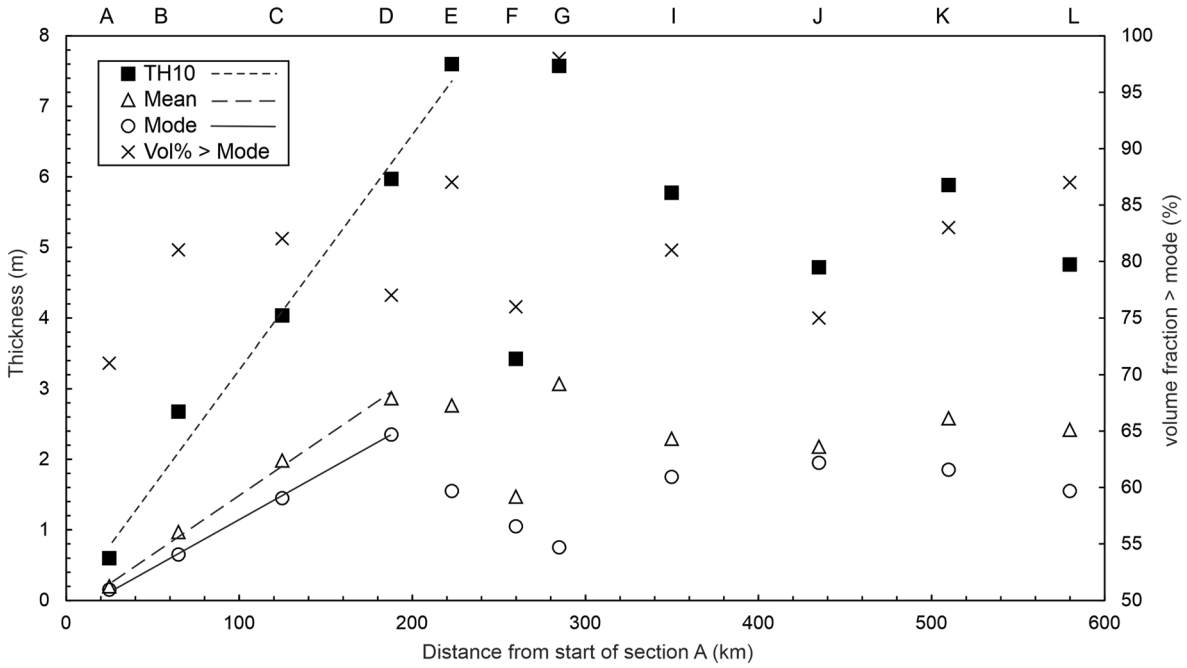

Figure 3. Key sea ice thickness statistics for sections in south-north direction with a linear fit for the first 190–220 km (also see supplementary information). For bimodal distributions, the second mode is plotted. Also plotted is the estimated total fraction of ice volume contained in deformed sea ice. Section H was flown west of G into Terra Nova Bay and is omitted from this plot.

convergent drift. The maximum thicknesses are much higher than expected from thermodynamic growth alone (Smith et al., 2012), indicating that significant dynamic processes are occurring in the area. The first mode of the Southern Profile is 0.15 m and is representative of thin, young ice in the MSP and TNBP (sections A, B, and H). Low percentages of open water in other sections can be associated with either active leads or leads which were refrozen and covered with thin nilas.

Near the transitions of the southern sections, we observe significant step changes between different ice regimes. Section A is the only area where the mode is similar to the mean, indicating a small amount of deformation. Both modal and mean ice thickness increase markedly at the transition to section B (Figure 2), which marks the transition from the relative shelter of McMurdo Sound to the wider Ross Sea area north of Ross Island. The mode is still relatively small (0.7 m), but T_{H10} is almost 4 times larger. The MODIS image in section B (Figure 1c) is relatively dark, indicating that this section is covered with thin thermodynamically grown ice interspersed with thick ice floes of dynamic origin. Passing Beaufort Island at the transition to section C we observe another rightward shift in the thickness distribution with the mean, mode and T_{H10} increasing by a factor of 2. In this section, only 100 km from the fast ice in McMurdo Sound, 44% of the measured ice thicknesses are greater than 2 m with a maximum recorded thickness of 8.25 m. Sections D, E, and G exhibit the highest values for T_{mean} and T_{H10}. Section E starts at a point just between Franklin Island and the terminus of the DIT, which formed a shear zone during the polynya event. This section includes a mixture of thick ice, as well as thinner, younger ice in its northern segment. The thickest ice on the Southern Profile is observed north and south of the DIT (>11 m in section E and G). The distribution of the Northern Profile is more uniform, but the thickest ice (>15 m) is observed in sections I, J, and K.

Of particular interest is the latitudinal change in sea ice thickness in the region. We describe this by plotting key statistics from section A through section L with the exception of section H avoiding complexity in the latitudinal thickness distribution via the TNBP (Figure 3). A near-linear increase for the mean, mode and T_{H10} is observed over the first 200 km of the Southern Profile. The maximum T_{H10} of the whole profile is also observed in section E (7.60 m), which is very similar to section G (7.58 m). The modal thicknesses for sections D, E, and G are within 0.30 m of one another, but the mean drops in section F because of the dramatic decrease in T_{H10}. The near-linear decrease in modal thickness from section D to G (Figure 3) can be explained by divergent flow, forcing the opening of leads and subsequent thin ice formation near the start of section F. The ice in F is likely younger than in E and G and not as heavily deformed. The drift trajectories near section E confirm that this ice is much older, originating in Zone 2, which was pushed against the coast before drifting to this position (Figure 1), whereas ice in section G originated in Zone 1. Apart from section F, northeast of DIT, the mean thickness north of section C remains higher than 2 m for the remainder of the latitudinal transect to the Adare Peninsula. The analyzed trajectories north of Cape Washington are oriented in a meridional direction, indicating that the ice, which has reached a maximum mean thickness around 75°S, is advected from the southern sections directly north parallel to the coast with no subsequent significant change in its mean thickness.

The sea ice regime of section H running east to west into Terra Nova Bay has been omitted from the analysis in Figure 3, as it is controlled by the TNBP. This 100 km long section is a mixture of extremely deformed ice at the eastern end, and very thin level polynya ice in the west. The relatively high percentage of open water (2.6%) is very thin ice in the west of Terra Nova Bay. There was no significant polynya event observed in the month before the survey flights, and the ice drift trajectories in the area suggest a slow and steady easterly drift pattern. Like the MSP, the thickness gradient cannot be explained by thermodynamic growth alone, but requires mechanical deformation as highlighted in a previous study (Hollands & Dierking, 2016). The eastern end of this profile is likely to be ice that has been repeatedly deformed.

From the visual inspection of high-resolution optical imagery, we attempt to draw conclusions about the proportion of ice volume in deformed ice (Figure S1). We find that major ridges can be identified if the width is at least 15 m, the maximum thickness is around 10 m or more, and the minimum thickness at the ridge margin is about 3 m. Taking the deformed volume fraction as $V_{D,3m}$, 15% of the length of the Southern Profile can be classified as major ridges holding 43% of the total ice volume (Figure 2).

Bimodal histogram distributions are a common feature originating from relatively large areas of thinner level ice interspersed with a network of thick ridges (sections C, D, E, I, J, K; Figure 1c). Calculating $V_{D,T\text{mode}2}$

for these regions, 75–87% of the ice volume is incorporated in deformed ice dominated by ridges (Figure 3). Some areas show unimodal distributions, either because of a high proportion of thin ice measurements in polynya areas (sections A and H), or the absence of larger regions of thin ice (sections B, F, and G). $V_{D,T\mathrm{mode}}$ for these regions is between 71% (section A) and 98% (section G and H). The local V_D minimum of section F (76%; $T_{\mathrm{mode}} = 1.05$ m) can be explained with a relatively large proportion of undeformed ice between here and the DIT. The high proportion of deformed ice in section A is due to increased thickness by rafting at the transition to section B. The bimodal distribution for the entire Southern profile (including section H) reveals $V_{D,T\mathrm{mode2}} = 80\%$ distributed over 48% (171 km) of the profile length.

The interpretation of the Northern profile is more difficult given the ice is older and its origin is more uncertain. There is a marked rightward shift in the distribution and very little thin ice is observed. Comparing the frequency histograms in Figure 2, it appears that the total observed ice volume is similar, but the second modal ice thickness has increased from 1.45 to 1.95 m. This suggests that all the thin ice has now been compacted into the heavily ridged pack ice. The low first mode for sections I and J (0.15 m) and the presence of open water is indicative of a divergent drift pattern in these sections just before the surveys. The largest ice thickness of the whole survey line (15.6 m) is observed in section K about 120 km south of the Adare Peninsula.

4. Context of Sea Ice Thickness Observations

By providing ice thickness information, we confirm the existence of a significant sea ice convergence zone in the western Ross Sea as suggested by Hollands and Dierking (2016). A polynya event at the beginning of October conditioned the observed sea ice morphology driving ice from the RSP directly toward the DIT and Terra Nova Bay. Assuming mass conservation, a uniform compression in size by 50% would have effectively doubled the mean sea ice thickness south of DIT by this single short-lived event. However, we find that within about 200 km from the start of the southern profile T_{H10} increases 1.9 and 2.3 times more strongly than T_{mean} and T_{mode}, respectively, suggesting that compression was not uniform but occurred preferentially along ridges. In the dynamically grown fast ice area south of the DIT, we can identify a combination of newly, heavily deformed ice embedded within much older ice. This implies that many ice floes in Zone 1 and two were already well developed and strong enough to withstand the pressure when pushed against each other and toward the coastline. Given the frequency of polynya events through winter, we assume that the sea ice, especially in Zones 1 and 2, has been subjected to multiple deformation events.

Our observations demonstrate that pack ice thickness in the western Ross Sea can increase over short spatial scales (100 km and less) to thicknesses greater than 2 m. The study has also revealed that the sea ice thickness in the western Ross Sea is much thicker than in the central Ross Sea despite the underestimation of thick ridges by AEM measurements (Jeffries & Adolphs, 1997). This general picture is supported by satellite observations between 2003 and 2008 with a thin ice area driven by the activity of the RSP with thicker ice adjacent to the west (Kurtz & Markus, 2012).

Satellite derived snow depths in the measurement area are mostly less than 10% of the observed ice thickness (Fons & Kurtz, 2019). Studies assuming an equality of freeboard and snow (e.g., Tian et al., 2020) therefore likely underestimate the ice thickness. A more detailed analysis of the airborne EM and coincident laser freeboard data would be required to explore this further.

Our measurements are only a snapshot in time but the processes leading to the thickness distributions reported here are frequently observed in the south-western Ross Sea (Dai et al., 2020; Hollands & Dierking, 2016). Apart from the area in the lee of Ross Island (sections A to C) we observed a distinct drift pattern transporting ice to the north. Common ice export estimates from the region, which are typically based on assumptions of thin ice in the whole area (Drucker et al., 2011; Ohshima et al., 2016), could be biased low in the west given the thickness distribution observed by us. The increasing trend in Ross Sea ice extent is highest for winter and spring (Parkinson, 2019), during a period when very thick sea ice of the western region is exported to the north. Near coastal reanalysis of wind and high-resolution sea ice drift in this area has been shown to be underestimated (Dale et al., 2017; Farooq et al., 2020), processes which are important to understand the thickness distribution we have observed. Large scale sea ice models need to be evaluated against observations and processes described in this study in order to fully explain volume trends in this region of sea ice growth.

5. Conclusions

The region's first direct assessment of ice thickness in the western Ross Sea reveals substantial deformation processes in a convergent sea ice regime. Ice was significantly thicker than expected from thermodynamic growth alone and further to the east in the central Ross Sea. A thickness of 16 m was measured in multiple sections along the flight profile north of Terra Nova Bay. Maximum thicknesses of narrow ridges are biased low because of the AEM signal footprint, which might explain lower maximum values along the Southern Profile compared to the north. From comparison with aerial photographs and satellite images, we conclude that ice preferentially grows in deformational ridges; about 43% of the sea ice volume in the area between McMurdo Sound and Terra Nova Bay is concentrated in more than 3 m thick ridges which cover about 15% of the Southern Profile. Our observations are in general agreement with the expected sea ice formation history in this important region driven by three major polynyas. Strong southerly winds with wind speeds up to 25 m s^{-1} in early October deformed the pack ice, which was surveyed one month later. The thickest 10% of ice increased sevenfold within 200 km from the McMurdo Sound Polynya, which persisted for the remaining 500 km north of Drygalski Ice Tongue. We only captured a relatively short longitudinal transect in Terra Nova Bay, but additional direct measurements across the complete Ross Sea are required to fully capture the ice thickness distribution in the region. Only then will it be possible to constrain the large uncertainties surrounding sea ice production and export in this important area of sea ice formation.

Data Availability Statement

Data used for this study are available from https://doi.org/10.1594/PANGAEA.925092.

Acknowledgments
The support by Antarctica NZ and the Italian Antarctic program (event K066) and the staff at Scott Base and Mario Zucchelli Base is greatly acknowledged. We particularly thank Johno Leitch and his team for excellent ground support for aircraft operations. This project would not have been possible without KBA BT67 crew Jamie Chisholm, Aaron Neyrinck, and Jan Verburg. This project was funded by the NZ Deep South National Science Challenge. D. Price was supported by the NZ Marsden Fund managed by the Royal Society.

References

Aulicino, G., Wadhams, P., & Parmiggiani, F. (2019). SAR pancake ice thickness retrieval in the Terra Nova Bay (Antarctica) during the PIPERS expedition in winter 2017. *Remote Sensing*, *11*(21), 2510. https://doi.org/10.3390/rs11212510

Brett, G. M., Irvin, A., Rack, W., Haas, C., Langhorne, P. J., & Leonard, G. H. (2020). Variability in the distribution of fast ice and the sub-ice platelet layer near McMurdo Ice Shelf. *Journal of Geophysical Research: Oceans*, *125*, e2019JC015678. https://doi.org/10.1029/2019JC015678

Coggins, J. H. J., McDonald, A. J., & Jolly, B. (2014). Synoptic climatology of the ross ice Shelf and ross sea region of Antarctica: k-Means clustering and validation. *International Journal of Climatology*, *34*, 2330–2348. https://doi.org/10.1002/joc.3842

Comiso, J. C., Kwok, R., Martin, S., & Gordon, A. L. (2011). Variability and trends in sea ice extent and ice production in the Ross Sea. *Journal of Geophysical Research*, *116*, C04021. https://doi.org/10.1029/2010JC006391

Dai, L., Xie, H., Ackley, S. F., & Mestas-Nuñez, A. M. (2020). Ice production in ross ice Shelf polynyas during 2017–2018 from sentinel-1 SAR images. *Remote Sensing*, *12*, 1484. https://doi.org/10.3390/rs12091484

Dale, E. R., McDonald, A. J., Coggins, J. H., & Rack, W. (2017). Atmospheric forcing of sea ice anomalies in the Ross Sea polynya region. *The Cryosphere*, *11*, 267–280. https://doi.org/10.5194/tc-11-267-2017

Drucker, R., Martin, S., & Kwok, R. (2011). Sea ice production and export from coastal polynyas in the Weddell and Ross Seas. *Geophysical Research Letters*, *38*, L17502. https://doi.org/10.1029/2011GL048668

Farooq, U., Rack, W., McDonald, A., & Howell, S. (2020). Long-term analysis of sea ice drift in the western Ross Sea, Antarctica, at high and low spatial resolution. *Remote Sensing*, *12*(9), 1402. https://doi.org/10.3390/RS12091402

Fons, S. W., & Kurtz, N. T. (2019). Retrieval of snow freeboard of Antarctic sea ice using waveform fitting of CryoSat-2 returns. *The Cryosphere*, *13*, 861–878. https://doi.org/10.5194/tc-13-861-2019

Haas, C., Hendricks, S., Eicken, H., & Herber, A. (2010). Synoptic airborne thickness surveys reveal state of Arctic sea ice cover. *Geophysical Research Letters*, *37*, L09501. https://doi.org/10.1029/2010GL042652

Haas, C., & Jochmann, P. (2003). Continuous EM and ULS thickness profiling in support of ice force measurements. In *Proceedings of the 17th international conference on port and ocean engineering under Arctic conditions POAC '03* (pp. 849–856). Trondheim, Norway. June 16–19, 2003.

Haas, C., Lobach, J., Hendricks, S., Rabenstein, L., & Pfaffling, A. (2009). Helicopter-borne measurements of sea ice thickness, using a small and lightweight, digital EM system. *Journal of Applied Geophysics*, *67*(3), 234–241. https://doi.org/10.1016/j.jappgeo.2008.05.005

Holland, P. R., & Kwok, R. (2012). Wind-driven trends in Antarctic sea-ice drift. *Nature Geoscience*, *5*, 872–875. https://doi.org/10.1038/ngeo1627

Hollands, T., & Dierking, W. (2016). Dynamics of the Terra Nova Bay polynya: The potential of multi-sensor observations. *Remote Sensing of Environment*, *187*, 30–48. https://doi.org/10.1016/j.rse.2016.10.003

Jeffries, M. O., & Adolphs, U. (1997). Early winter ice and snow thickness distribution, ice structure and development of the western Ross Sea pack ice between the ice edge and the Ross Ice Shelf. *Antarctic Science*, *9*(2), 188–200 https://doi.org/10.1017/S0954102097000242

Kaleschke, L., Tian-Kunze, X., Maaß, N., Mäkynen, M., & Drusch, M. (2012). Sea ice thickness retrieval from SMOS brightness temperatures during the Arctic freeze-up period. *Geophysical Research Letters*, *39*, L05501. https://doi.org/10.1029/2012GL050916

Kern, S. (2009). Wintertime Antarctic coastal polynya area: 1992–2008. *Geophysical Research Letters*, *36*, L14501. https://doi.org/10.1029/2009GL038062

Kurtz, N. T., & Markus, T. (2012). Satellite observations of Antarctic sea ice thickness and volume. *Journal of Geophysical Research*, *117*, C08025. https://doi.org/10.1029/2012JC008141

Mackie, S., Langhorne, P. J., Heorton, H. D. B. S., Smith, I. J., Feltham, D. L., & Schroeder, D. (2020). Sea ice formation in a coupled climate model including grease ice. *Journal of Advances in Modeling Earth Systems*, *12*, e2020MS002103. https://doi.org/10.1029/2020MS002103

Nakata, K., Ohshima, K. I., Nihashi, S., Kimura, N., & Tamura, T. (2015). Variability and ice production budget in the Ross Ice Shelf Polynya based on a simplified polynya model and satellite observations. *Journal of Geophysical Research: Oceans*, *120*, 6234–6252. https://doi.org/10.1002/2015JC010894

Ohshima, K. I., Nihashi, S., & Iwamoto, K. (2016). Global view of sea-ice production in polynyas and its linkage to dense/bottom water formation. *Geoscience Letters*, *3*, 13. https://doi.org/10.1186/s40562-016-0045-4

Parkinson, C. L. (2019). A 40-y record reveals gradual Antarctic sea ice increases followed by decreases at rates far exceeding the rates seen in the Arctic. *Proceedings of the National Academy of Sciences of the United States of America*, *116*(29), 14414–14423. https://doi.org/10.1073/pnas.1906556116

Paul, S., Hendricks, S., Ricker, R., Kern, S., & Rinne, E. (2018). Empirical parametrization of envisat freeboard retrieval of Arctic and Antarctic sea ice based on CryoSat-2: Progress in the ESA climate change initiative. *The Cryosphere*, *12*(7), 2437–2460. https://doi.org/10.5194/tc-12-2437-2018

Pfaffling, A., Haas, C., & Reid, J. E. (2007). Direct helicopter EM—Sea-ice thickness inversion assessed with synthetic and field data. *Geophysics*, *72*(4), F127–F137. https://doi.org/10.1190/1.2732551

Price, D., Beckers, J., Ricker, R., Kurtz, N., Rack, W., Haas, C., et al. (2015). Evaluation of CryoSat-2 derived sea-ice freeboard over fast ice in McMurdo Sound, Antarctica. *Journal of Glaciology*, *61*(226), 285–300. https://doi.org/10.3189/2015JoG14J157

Price, D., Soltanzadeh, I., Rack, W., & Dale, E. (2019). Snow-driven uncertainty in Cryosat-2-derived Antarctic sea ice thickness—Insights from McMurdo Sound. The *Cryosphere*, *13*(4), 1409–1422. https://doi.org/10.5194/tc-13-1409-2019

Reid, J. E., Pfaffling, A., & Vrbancich, J. (2006). Airborne electromagnetic footprints in 1D earths. *Geophysics*, *71*(2), G63–G72. https://doi.org/10.1190/1.2187756

Smethie, W. M., Jr, & Jacobs, S. S. (2005). Circulation and melting under the ross ice Shelf: Estimates from evolving CFC, salinity and temperature fields in the ross sea. *Deep Sea Research I: Oceanographic Research Papers*, *52*(6), 959–978. https://doi.org/10.1016/j.dsr.2004.11.016

Smith, I. J., Langhorne, P. J., Frew, R. D., Vennell, R., & Haskell, T. G. (2012). Sea ice growth rates near ice shelves. *Cold Regions Science and Technology*, *83*(84), 57–70. https://doi.org/10.1016/j.coldregions.2012.06.005

Tamura, T., Ohshima, K. I., Fraser, A. D., & Williams, G. D. (2016). Sea ice production variability in Antarctic coastal polynyas. *Journal of Geophysical Research: Oceans*, *121*, 2967–2979. https://doi.org/10.1002/2015JC011537

Thorndike, A. S., Rothrock, D. A., Maykut, G. A., & Colony, R. (1975). The thickness distribution of sea ice. *Journal of Geophysical Research*, *80*(33), 4501–4513. https://doi.org/10.1029/jc080i033p04501

Tian, L., Xie, H., Ackley, S., Tang, J., Mestas-Nuñez, A., & Wang, X. (2020). Sea-ice freeboard and thickness in the Ross Sea from airborne (IceBridge 2013) and satellite (ICESat 2003–2008) observations. *Annals of Glaciology*, *61*(82), 24–39. https://doi.org/10.1017/aog.2019.49

Uotila, P., Goosse, H., Haines, K., Chevallier, M., Barthélemy, A., Bricaud, C., et al. (2019). An Assessment of ten ocean reanalyzes in the polar regions. *Climate Dynamics*, *52*(3), 1613–1650. https://doi.org/10.1007/s00382-018-4242-z

Van Woert, M. L. (1999). Wintertime dynamics of the Terra Nova Bay polynya. *Journal of Geophysical Research*, *104*(C4), 7753–7769. https://doi.org/10.1029/1999JC900003

Weeks, W. F., Ackley, S. F., & Govoni, J. (1989). Sea ice ridging in the Ross Sea, Antarctica, as compared with sites in the Arctic. *Journal of Geophysical Research*, *94*(C4), 4984–4988. https://doi.org/10.1029/JC094iC04p04984

Williams, G., Maksym, T., Wilkinson, J., Kunz, C., Murphy, C., Kimball, P., & Singh, H. (2015). Thick and deformed Antarctic sea ice mapped with autonomous underwater vehicles. *Nature Geoscience*, *8*, 61–67. https://doi.org/10.1038/NGEO2299

Worby, A. P., Geiger, C. A., Paget, M. J., Van Woert, M. L., Ackley, S. F., & DeLiberty, T. L. (2008). Thickness distribution of Antarctic sea ice. *Journal of Geophysical Research*, *113*, C05S92. https://doi.org/10.1029/2007JC004254